Broadband and Spectrally Selective Photothermal Conversion through Nanocluster Assembly of Disordered Plasmonic Metasurfaces

Ji-an Chen[1,2,†], Yuyuan Qin[1,2,†], Yubiao Niu[3,6], Peng Mao[1,2]*, Fengqi Song[1], Richard E Palmer[3], Guanghou Wang[1], Shuang Zhang[4,5] and Min Han[1,2]*

1. National Laboratory of Solid-State Microstructures and Collaborative Innovation Centre of Advanced Microstructures, Nanjing University, Nanjing 210093, China

2. College of Engineering and Applied Sciences and Jiangsu Key Laboratory of Artificial Functional Materials, Nanjing University, Nanjing 210023, China

3. Nanomaterials Lab, Faculty of Science and Engineering, Bay Campus, Swansea University, Swansea SA1 8EN, UK

4. Department of Physics, University of Hong Kong, Hong Kong 999077, China.

5. Department of Electrical and Electronic Engineering, University of Hong Kong, Hong Kong 999077, China

6. Nium Ltd. Research Complex at Harwell (RCaH) Rutherford Appleton Laboratory Harwell, Oxfordshire OX11 0FA, UK

*Email: Peng Mao pmao@nju.edu.cn; Min Han sjhanmin@nju.edu.cn

ABSTRACT: Plasmonic metasurfaces have been realized for efficient light absorption, thereby leading to photothermal conversion through non-radiative decay of plasmonic modes. However, current plasmonic metasurfaces suffer from inaccessible spectral ranges, costly and time-consuming nano-lithographic top-down techniques for fabrication, and difficulty of scale-up. Here, we demonstrate a new type of disordered metasurface created by densely packing plasmonic nanoclusters of ultra-small size on a planar optical cavity. The system either operates as a broadband absorber or offers a reconfigurable absorption band right across the visible region, resulting in continuously wavelength-tunable photothermal conversion. We further present a method to measure the temperature of plasmonic metasurfaces via surface-enhanced Raman spectroscopy (SERS), by incorporating single-walled carbon nanotubes (SWCNTs) as a SERS probe within the metasurfaces. Our disordered plasmonic system, generated by a bottom-up process, offers excellent performance and compatibility with efficient photothermal conversion. Moreover, it also provides a novel platform for various hot-electron and energy-harvesting functionalities.

KEYWORDS: plasmonic metasurface, nanocluster assembly, photothermal conversion, SERS, disordered nanostructure, light absorber

The oscillation of charge carriers at the surfaces of metallic nanostructures, known as localized surface plasmon resonances (LSPRs)—can confine light on the nanoscale and strongly enhance the light-matter interactions[1]. Once launched, plasmons can decay via either radiative or non-radiative processes[2]. In the non-radiative process, hot electrons are generated inside the metals, which can be harvested by Schottky Junctions. The internal decay of hot electrons inside the metallic nanostructure can lead to significant heating of the nanostructure itself, as well as its immediate environment[2-5]. The ability to effectively heat, and to measure the nanostructure's temperature, has resulted in some interested plasmonics applications, including photothermal nanotherapeutics[6], heterogeneous catalysis[7-14], drug delivery[15], photothermal melting of DNA[16], and steam generation[17-19].

Plasmonic metasurfaces represent an intriguing class of plasmonic systems for photothermal conversion and offer a basis for groundbreaking innovations in various areas [3, 20-22]. Metasurfaces are artificial materials comprised of arrays of optical antennas with subwavelength dimensions, allowing for unparalleled control of electromagnetic waves to overcome the limitations of naturally occurring optical materials[23-26]. However, the desirable absorption spectral features, such as broadband absorption and strong spectral selectivity are seldom found in intrinsic materials. In contrast, metasurfaces based on metallic nanostructures can be designed to realize high-efficiency absorption for nearly any wavelength by leveraging the unique properties of metallic nanostructures [27-28]. Through judicious design, metamaterials can facilitate the coupling of multiple modes, such as LSP (localized surface plasmon)-LSP coupling[29], LSP-SPP (surface plasmon polariton) coupling[30], and LSP-cavity coupling[31]. This, in turn, can increase light absorption and enhance photothermal conversion. Amongst various types of metamaterials, metal-insulator-metal (MIM) type metasurfaces have been extensively studied and used for photothermal conversion due to their near-perfect absorption and tunable wavelength selectivity [32-33]. However, achieving both spectral-selective and broadband absorption in the same metamaterial platform is usually not feasible. Moreover, such MIM metasurfaces typically consist of a periodic array of nanoscale resonators, which need to be patterned by time-consuming and costly nanolithography techniques, such as focused ion beam (FIB) lithography and electron beam lithography (EBL)[32-34].

In this paper, we utilize our recently developed strategy, based on disordered plasmonic metasurfaces, to achieve highly efficient photothermal conversion over either a broadband region

or a selected narrowband region [35-36]. The disordered plasmonic metasurface comprises of nanometre-sized Au nanoclusters with randomised sizes and positions, providing the necessary disorder. The nanoclusters are deposited on a dielectric spacer above a silver film, forming a Fabry-Perot-like system. Interestingly, by controlling the thickness of the dielectric spacer, the disordered plasmonic system experiences a phase transition, from a system with broadband absorption to one with a finite absorption band with the peak ranging from 400 to 800 nm. Thus efficient broadband photothermal conversion and selected narrowband photothermal conversion can be achieved on the same platform. Infrared (IR) thermal imaging and SERS spectroscopy are used to investigate the heat generated at the surface of absorbers, and to quantify the local temperature increase induced by laser illumination, respectively. Importantly, this new type of disordered MIM-type metasurface can be fabricated by a facile gas-phase nanocluster beam deposition method, without requiring sophisticated and/or time-consuming lithography processes.

Sample design and theoretical simulations

The disordered metasurface system we designed is composed of nanometre-sized Au nanoclusters with randomized size and position on a lossless dielectric spacer layer with controlled thickness, which is situated on top of an opaque Ag film, as illustrated in Figure 1(a). Based on coupled mode theory (CMT), we can use a generalized model to describe a simple cavity supporting a specific resonant mode, which has a certain coupling rate to the free space and an intrinsic decay rate. The critical coupling for reaching complete absorption occurs when the two rates match each other, a mechanism similar to the impedance matching in electronic systems. The physical details of this model can be found in our previous works [36]. Different from traditional plasmonic nanostructures and MIM-type periodic metamaterials [2, 20], the disordered plasmonic metasurface has the ability to achieve either broadband absorption or selective limited bandwidth reflection based on the desired application. When the dielectric spacer thickness is too small to support any Fabry-Perot modes in the visible, the disordered plasmonic system exhibits broadband absorption, owing to the disorder-induced energy equipartition. However, when a certain optical mode can be supported by the system, the mismatch between the coupling rate and the intrinsic decay rate causes the optical mode to be reflected rather than absorbed, resulting in limited band reflection as desired. It is worth mentioning that our disordered plasmonic system reverses the absorption/reflection property of the cavity. Specifically, when the photons on resonance with the

cavity, they are reflected back in a disordered system, while a pure Fabry-Perot cavity always absorbs the photons around its resonance.

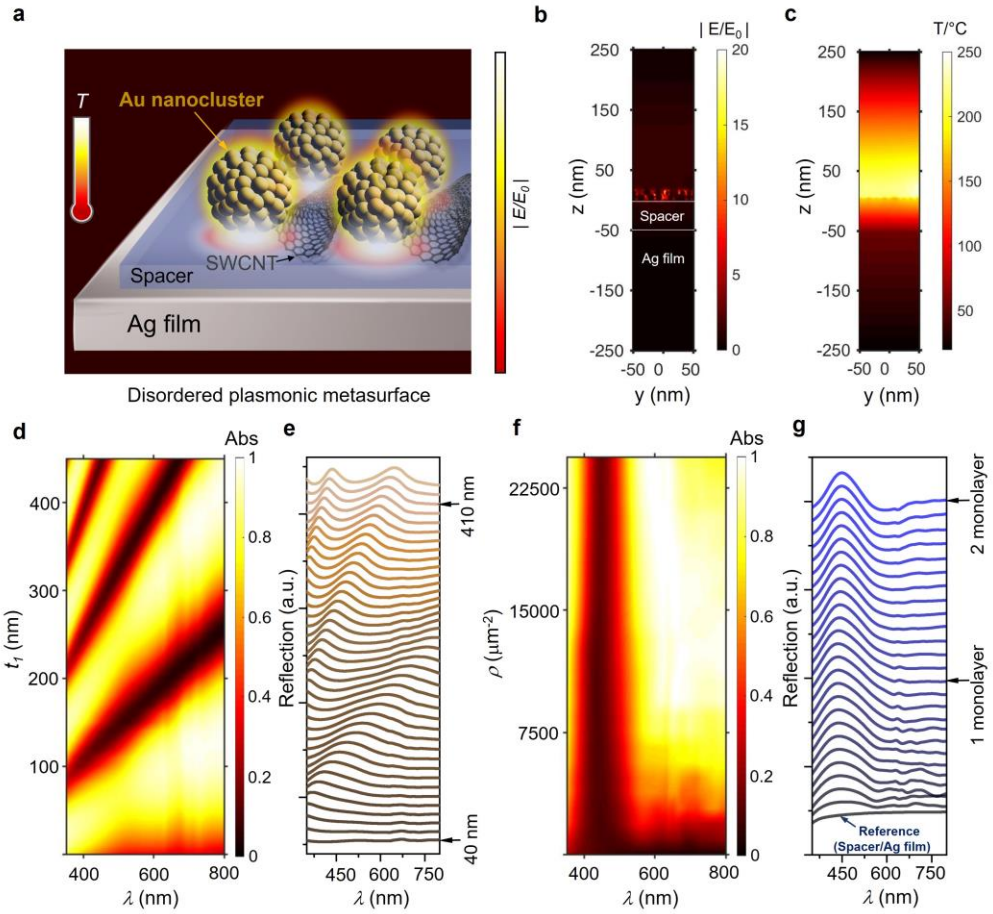

Figure 1. Numerical simulations for the disordered plasmonic metasurface. (a) Schematic diagram of the geometric structure and material composition of the designed three-layer metasurface. Electric field intensity (b) and temperature field (c) spatial distributions of the disordered metasurface (spacer thickness, t_1=50 nm), which were calculated by using Finite-Difference Time-Domain (FDTD) and Finite Element Method (FEM) methods, respectively. A plane wave is launched at z = 200 nm along the z direction with a wavelength of 633 nm and an intensity of 7 mW/μm^2. The corresponding absorption (d) and reflection spectra (e) as a function of spacer thickness from FDTD simulations. The corresponding absorption (f) and reflection spectra (g) as a function of nanocluster density from FDTD simulations.

We next employ 3D FDTD full-wave simulations to clarify the optical absorption and photothermal conversion of the disordered plasmonic system. Figure 1(b) shows the electric field distribution of an optimized disordered plasmonic metasurface consisting of Au nanocluster ($d = 12\ nm, \delta = 2\ nm$) /LiF ($t_1 = 60\ nm$)/Ag film ($t_2 = 200\ nm$), where the parameter δ describes the degree of disorder (Figure S1-S5). Broadband absorption is shown in Figure 1(b) with most photons trapped inside the metasurface. Through the creation of hot electrons via Landau damping, the non-radiative decay of hot electrons inside the nanoclusters can lead to significant heating of

the nanoclusters themselves and the immediate environment, significantly boosting the temperature around metal nanoclusters. The Joule heating can be described as [37]

$$Q(r) = \frac{\omega}{2}\varepsilon_0 \mathrm{Im}(\varepsilon_\omega) \int_V |E_\omega|^2 \, \mathrm{d}r \qquad (1)$$

where *Q(r)* is the heat source density, ω is the optical frequency, ε_0 is the dielectric permittivity in a vacuum, ε_ω is the relative permittivity of the metasurface. After the heat generation, the heat transfer process that lasts in picoseconds can be described as [38]

$$\rho C_P \frac{\partial T}{\partial t} + \nabla \cdot [\kappa \nabla T] = -Q \qquad (2)$$

where ρ is the mass density, C_p is the thermal capacity, and κ is the thermal conductivity. Thus, the steady-state temperature field distribution of the metasurface is obtained by combining eq 1 and eq 2 [39], with the results shown in Figure 1(c). Figure 1(d-e) shows how the absorption and reflection spectra are expected to vary with changes in the thickness of the dielectric spacer. This disordered plasmonic system exhibits a broadband absorption when the spacer thickness is around 40 nm to 60 nm, while gradually evolving into a redshifted narrowband reflection when the spacer thickness increases from 60 nm to 450 nm, enabling a spectrally selective absorption in the visible. Figure 1(f-g) plots the absorption and reflection spectra of metasurfaces with different nanocluster densities from 0 to 25000 μm^{-2}. The bandwidth of the reflection peak decreases with growing nanoclusters density, while the nanocluster density is greater than ~10000 μm^{-2}, the spectral feature no longer changes significantly. These results indicate that choosing nanocluster density also can regulate the absorption and thus photothermal conversion of the metasurface at a specific wavelength.

Experimental realization of the disordered plasmonic metasurfaces

Experimentally, the proposed metasurfaces are realized by using the following procedure (Figure S6). First, the Ag film with a thickness of 200 nm was coated on a silica wafer through a thermal evaporation process. This Ag film functions as an optically thick mirror, which reflects more than 97% of the incident light at the wavelength range of 400 nm to 800 nm. Next, a dielectric spacer layer (LiF or Al_2O_3) was grown on the surface of the mirror. Finally, a novel gas-phase cluster beam technique was employed to produce Au nanoclusters on the top of the cavity (dielectric/mirror) [35, 36, 40-41]. Figure 2(a-b) show the scanning electron microscopy (SEM) images of the cross-sectional view and top view of the fabricated structure, respectively. The SEM images

clearly show the disorder in both the shape and position of the nanoclusters. For a quantitative illustration of the disorder, we further performed a two-dimensional Fast Fourie Transform (2D-FFT) of the image of Au nanoclusters. A circular distribution in the squared Fourier components is observed in the inset of Figure 2(b), confirming the random arrangement of the Au nanoclusters [42]. Figure 2(c) provides a scanning transmission electron microscopy (STEM) image of a single Au nanocluster, revealing the high quality of the Au nanoclusters produced by the gas-phase cluster beam deposition technique. Figure 2(d) shows the size distribution of an optimized sample, which follows a Log-Normal distribution with an average value of 11.8 nm.

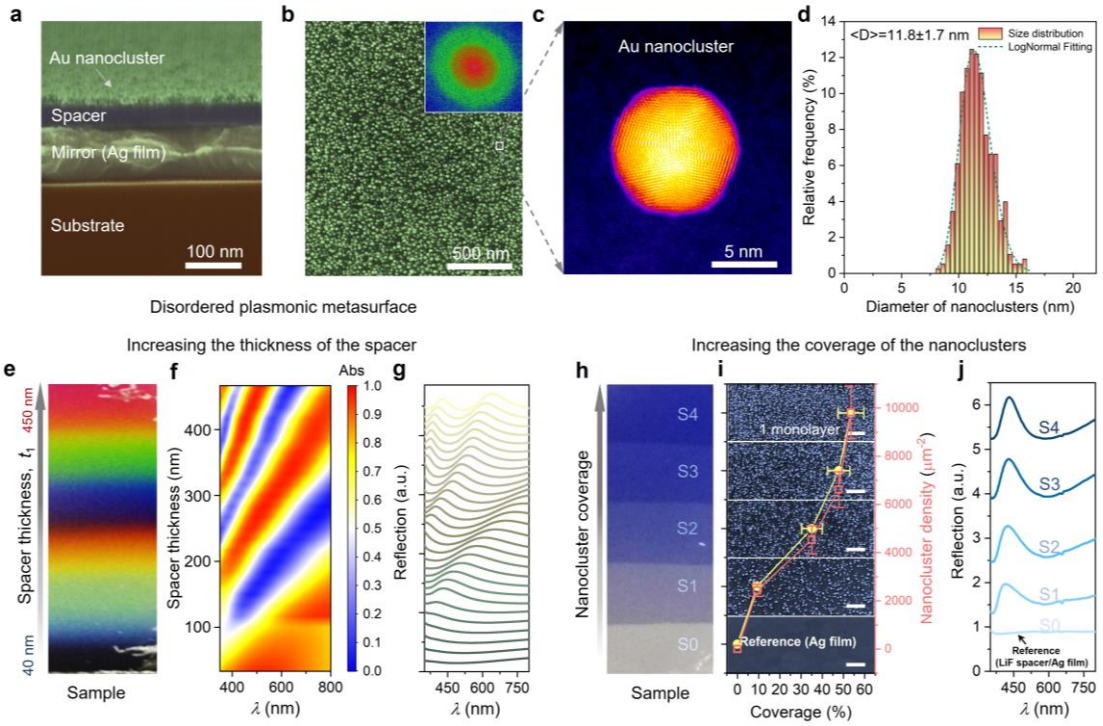

Figure 2. Experimental realisation of the disordered plasmonic system. (a) A cross-sectional view and (b) a top-view SEM image of the sample. Inset: 2D-FFT of the image of Au nanoclusters. nanoclusters (c) STEM image of a single Au nanocluster. (d) Size distribution histogram of the Au nanoclusters in the optimized disordered metasurface and corresponding Log-Normal fitting. (e) Photographic picture of the sample with gradually varying spacer thickness along the vertical direction. The corresponding absorption (f) and reflection spectra (g) of the sample. (h) A photographic image illustrating the colour generation from the sample with different nanocluster densities. (i) SEM images and nanocluster coverages for the sample with four different nanocluster densities. Scale bar, 100nm. (j) The corresponding reflection spectra for the sample with different nanocluster densities.

To show the range of optical absorption achievable with such a disordered system, we vary the thickness of the LiF spacer layer spatially on a single sample (Figure S7) in which the dielectric LiF spacer has a thickness that varies continuously from 40 to 450 nm. Figure 2(e) provides a photographic image of the sample. The corresponding colour map of the absorption spectra and

reflection spectra are shown in Figure 2(f-g), respectively. Starting from a small thickness (~ 40 to 60 nm), broadband absorption is achieved owing to the equipartition of energy. With further increase of the spacer thickness, the system enters the regime of tunable reflection/absorption, leading to a band with red-shifted reflection peaks, agreeing with the simulated results. In addition, we also experimentally demonstrate that the absorption/reflection of the disordered system can be tuned by changing the nanocluster density. We fabricate metasurfaces with different Au nanocluster densities with coverage (the proportion of the surface area that is covered by nanoclusters) of 9.3%, 35.1%, 47.8% and 53.5%. The corresponding nanocluster density is 2439 μm^{-2}, 4537 μm^{-2}, 6615 μm^{-2} and 9823 μm^{-2}, respectively (Figure S8). The right-hand panel of Figure 2(h) shows a picture of the samples with the colour shining more brilliantly as the density increases. As the density increases, the near-field coupling strength grows nonlinearly, intensifying the disorder embedded in the system [36]. Figure 2(i) plots the reflection spectra of the sample with four different densities. Note that the bandwidth of reflection shrinks and absorptance increases with increasing density (disorder), agreeing with the numerical result shown in Figure 1(f-g), and agreeing with the results shown in our previous Ag nanocluster/spacer/mirror system [36].

Broadband and Wavelength-selective photothermal conversion of the disordered plasmonic metasurfaces

The wavelength flexibility of the disordered metasurface allows for the spectrally selective photothermal conversion to be engineered. Here, we demonstrate the superiority of this approach, four typical large-area metasurfaces were fabricated with different resonance absorption in the visible regime (Figure 3(a)). Figure 3(b) presents the photothermal performance of the metasurfaces under laser illumination in an open environment, each sample was illuminated by 405 nm, 473 nm, 532 nm, and 660 nm continuous-wave (CW) laser respectively, with a power density of about 100 $mW \cdot cm^{-2}$. While illuminating the samples, we used a thermal imaging camera to record the surface temperature of the samples. For the black-coloured metasurface with broadband absorption, the temperature increased from room temperature (T_0=23°C) to 56.7°C, 57.4°C, 60.4°C and 57.7°C, under the illumination of 405 nm, 473 nm, 532 nm, and 660 nm lasers, respectively, which demonstrate an efficient photothermal conversion of the sample within the broadband regime. In contrast, the maximum temperature change of the blue-, green-, and red-coloured samples shows a strong correlation with the absorption band of the three samples, the

samples will be heated only when the laser wavelength matches the absorption band of the metasurfaces, as shown in Figure 3(b). The reflection spectra for these four metasurfaces are shown in Figure 3(c), and the extracted temperature increments ($\Delta T=T-T_0$) are plotted in Figure 3(d), distinctly showing the broadband photothermal conversion and spectrally selective photothermal conversion of the samples. To highlight the feasibility of the spectrally selective photothermal conversion of the metasurface, we prepared a set of 'NJU' patterns with coloured metasurfaces (Figure S9). Three sets of infrared images were captured under the illumination of 473 nm, 532 nm, and 660 nm lasers, respectively. As shown in Figure 3(e), the letter 'N', 'J', and 'U' has the lowest temperature when the laser wavelength matches the reflection band of the metasurfaces.

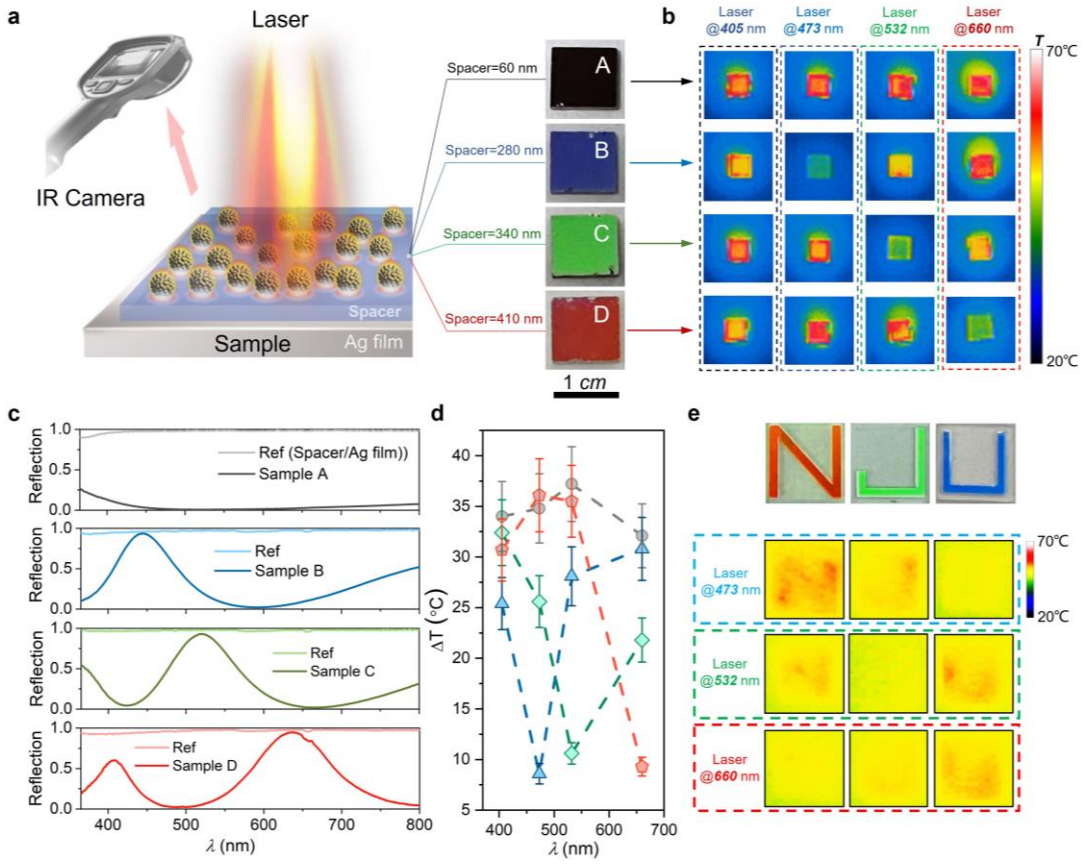

Figure 3. Optical Characterization and photothermal observation of the disordered plasmonic metasurfaces. (a) Left: Schematic representation of IR thermal imaging process for the samples. Right: Photographs of four metasurface samples with broadband reflection or reconfigurable reflection, where the metasurfaces are fabricated with 60 nm, 280nm, 340nm and 410 nm spacer layers**.** To achieve maximum light absorption, the nanoclusters on the metasurfaces are controlled to 2 monolayers. (b) Thermal image of the four metasurfaces under illumination by 405 nm, 473 nm, 532 nm and 633 nm laser. The corresponding reflection spectra (c) and extracted temperature increments (ΔT) (d) for the four samples. (e) Top: optical images of 'NJU' patterns with three different coloured metasurfaces.

Bottom: IR images of 'NJU' patterns under the illumination of 473 nm, 532 nm, and 660 nm lasers.

Photothermal conversion of the disordered metasurface studied by surface-enhanced Raman spectroscopy (SERS)

Raman spectroscopy has been applied for temperature assessment, by using the intensity ratio change of the Stokes and anti-Stokes Raman peaks with temperature or the frequency change of some materials such as silicon, gallium nitride, carbon nanotubes, and graphene as a result of the lattice expansion and compression [43-46]. By incorporating plasmonic enhancements and localized hot-spots in Raman measurements, commonly known as surface- or tip-enhanced Raman spectroscopy (SERS or TERS), we anticipate a significant augmentation in the intensity of Raman signals, leading to a substantial improvement in temperature measurement resolution. We develop an indirect method to measure the temperature right at the surface of the metasurfaces by using the SERS frequency shift of the vibration of carbon atoms along the nanotube axis direction of single-walled carbon nanotube (SWCNT) adsorbed on the disordered metasurfaces (Figure S10). The SERS experiment was performed with a very low laser power (100 μW) using 633 nm as the excitation source to avoid the heating effect of the laser (Figure S11). The metasurface exhibits superior SERS performance compared to the reference substrate, with a signal intensity 1300 folds better (Figure 4(a)). This enhancement occurs due to the excitation of plasmonic modes and thus induces large field enhancement in the metasurface (Figure S12). Distinct peaks can be observed in the low ($\omega \leq 500$ cm^{-1}), mid ($500 \leq \omega \leq 1800$ cm^{-1}) and high ($\omega \geq 1800$ cm^{-1}) frequency regions of the spectra. Unlike graphite and graphene, the G band of SWCNT, which is located in the mid-frequency region arises due to the zone folding of the graphene. Brillouin zone and the G band is a triplet with Raman active A_{1g}, E_{1g} and E_{2g} symmetries [46]. Therefore, the G band is best fitted by six peaks at about 1540, 1542, 1561, 1583, 1592 and 1602 cm^{-1} (Figure 4b), and these peaks are identified as $A(A_{1g})$, $E_2(E_{2g})$, $A(A_{1g})+E_1(E_{1g})$, $A(A_{1g})$, $A(A_{1g})+E_1(E_{1g})$ and $E_2(E_{2g})$, respectively [47]. The low (ω_G^-) and high (ω_G^+) frequency side of the G band is associated with the vibration of carbon atoms along the circumferential and the nanotube axis direction, respectively [48]. As is shown in Figure 4(b), the G^+ peak that appears at 1591 cm^{-1} is the most intense peak of SWCNT, so it is most feasible to use ω_G^+ as a criterion for temperature increase.

In order to check the possibility of using the frequency shift of SWCNT for temperature sensing, we first investigated the temperature-dependent Raman behaviours of SWCNTs adsorbed on the

SiO_2 substrate surface, as shown in Figure 4(c). Figure 4(d) shows the temperature-dependent G^+ peak extracted from the Raman spectra of SWCNT-SiO_2. G^+ peak has a frequency redshift because of softening of force constant upon temperature increase [49]. The G^+ shows a very good linear dependence on the temperature (Figure 4(e)), so that the data is best fitted by considering the following linear equation $\omega = \omega_0 + \alpha T$, where ω_0 is the frequency at 0 ℃, and α is the first order temperature coefficient. The calculated average value of α_{G+} is about 0.01608 $cm^{-1}/℃$, which is very close to that using the frequency shift in SWCNT or silicon cases [50-51].

Using the temperature calibration obtained above, we can then quantitatively extrapolate the temperature increase under the photothermal effect. We first measured the Raman shift of bare SWCNT on an Ag mirror with increasing laser power from 1 mW to 7 mW at 633 nm (Figure 4(f)), $\omega_G{}^+$ shows a redshift of 0.5 cm^{-1}, as shown in Figure 4(g). The data recorded shows that G mode has undergone monotonous red-shifting and broadening with an increase in laser power. The changes above in the Raman line shape suggest that the increase in laser power has significantly increased the temperature. Typically, we achieve a temperature increase in SWCNT on bare mirror rises by 30 ℃ under a 7 mW laser illumination (Figure 4(h-k)), which results from the low absorption of SWCNT and reflective mirror.

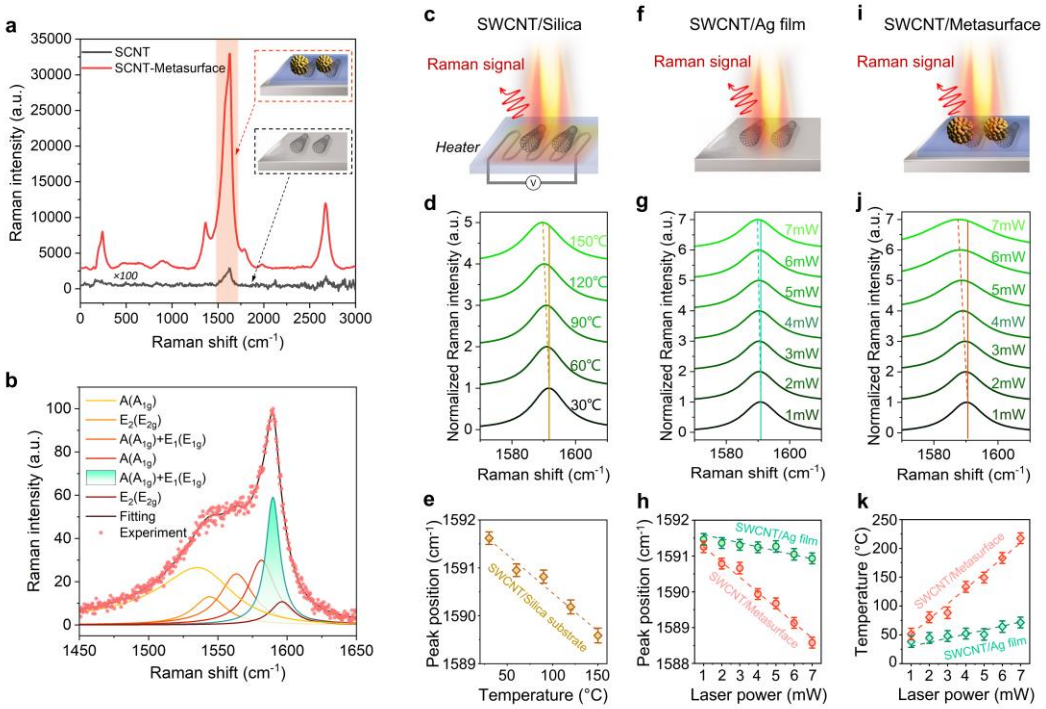

Figure 4. Temperature detection using SWCNTs adsorbed on the disordered metasurface. (a) SERS spectra were measured from the SWCNT-metasurface and SWCNT-smooth Ag film (reference).

(b) The G band fits with six peaks. (c) Schematic of temperature-dependent Raman measurement. (d) Temperature-dependent G^+ peak extracted from Raman spectra of SWCNT. (e) Raman shifts of G^+ peak as a function of temperature. (f) Schematic of laser power-dependent SERS measurement. (g) Laser power-dependent G^+ peak extracted from SERS spectra of SWCNT-smooth Ag film. (h) Raman shift of the G^+ peak as a function of laser power. (i) Schematic of laser power-dependent SERS measurement. (j) Laser power-dependent G^+ peak extracted from SERS spectra of SWCNT-metasurface. (k) The measured temperature as a function of laser power. All the Raman measurements are conducted in the air.

Next, we investigate the temperature increase induced by laser illumination in the metasurface with an Al_2O_3 spacer thickness of 45 nm (Figure 4(i)), which can absorb nearly 90% of the incident light at 633 nm. This broadband plasmonic metasurface enables optical trapping and efficiently generates rapid and significantly elevated temperatures within the metasurface. The shift of the G^+ peak, relative to the laser intensity, is illustrated in Figure 4(j), allowing us to calculate the corresponding temperature increase as a function of laser power. Notably, each 1 mW increment in laser power leads to a temperature rise of 28 ℃ (Figure 4(h-k)). Furthermore, the metasurface exhibits remarkable stability in the photothermal conversion cycle, owing to the robust optical properties of the disordered system (Figure S13-S14).

In conclusion, we proposed, modelled and experimentally demonstrated a novel disordered plasmonic metasurface based on metal nanoclusters/dielectric spacer/metal film multiple structures for efficient light absorption and excellent absorption tunability in the visible range. By tailoring the spacer thickness, wavelength-tunable absorption can be achieved in the whole visible range. Realizing considerably higher photothermal conversion efficiency, either over a broadband region or a selected narrowband region. Apart from its theoretical importance, the metasurface we proposed here can be easily prepared by the gas-phase cluster beam deposition method, without any sophisticated and/or time-consuming lithography processes. Moreover, we proposed a method of using SWCNT adsorbed on the metasurface for accurate heat sensing based on the SERS technique. This work offers a feasible solution and a design principle for the development of cost-effective metasurface absorbers using bottom-up methods.

Supporting Information

The Supporting Information is available free of charge at http://pubs.acs.org.

FDTD and FEM simulation details, experimental details, results and discussion (materials

fabrications, characterizations, optical measurements, Raman measurements, temperature detecting by using SERS technique, results and discussion), and Figures S1–S14 (PDF)

Author Contributions

† J. C and Y. Q. contributed equally to this work. P.M., S.Z. and M.H. conceived the project ideas. P.M., J.C., Y. Q and Y. N. performed experiments and sample characterizations. P.M. and J.C. developed the model and performed numerical simulations and data analysis. P.M. wrote the manuscript with input from J. C., Y. Q., Y. N., F. S., R. E. P., G. W., S. Z. and M. H.. F. S., R. E. P., G. W., S. Z. and M. H. supervised the project. All authors discussed the results.

Acknowledgments

We are grateful for the financial support from the National Natural Science Foundation of China (Grant No. 12274213, 12104220, 11627806 and U1909214), the National Key R&D Program of China (Grant No. 2016YFA0201002), and the Funded by Open Foundation of the State Key Laboratory of Fluid Power and Mechatronic Systems (Grant No. GZKF-202217).

Reference

[1] Maier, S.A., *Plasmonics: fundamentals and applications*. Vol. 1. 2007: Springer.

[2] Brongersma M L, Halas N J, Nordlander P. Plasmon-induced hot carrier science and technology. ***Nature Nanotechnology***, 2015, 10(1), 25-34.

[3] Chen, J., Ye, Z., Yang, F., & Yin, Y. Plasmonic nanostructures for photothermal conversion. ***Small Science***, 2021, 1(2), 2000055.

[4] Linic S, Chavez S, Elias R. Flow and extraction of energy and charge carriers in hybrid plasmonic nanostructures. ***Nature Materials***, 2021, 20(7), 916-924.

[5] Clavero, C. Plasmon-induced hot-electron generation at nanoparticle/metal-oxide interfaces for photovoltaic and photocatalytic devices. ***Nature Photonics***, 2014, 8(2), 95-103.

[6] Ha, M., Nam, S. H., Sim, K., Chong, S. E., Kim, J., Kim, Y., ... & Nam, J. M. Highly efficient photothermal therapy with cell-penetrating peptide-modified bumpy Au triangular nanoprisms using low laser power and low probe dose. ***Nano Letters***, 2020, 21(1), 731-739.

[7] Zhou L, Swearer D F, Zhang C, et al. Quantifying hot carrier and thermal contributions in plasmonic photocatalysis. ***Science***, 2018, 362(6410), 69-72.

[8] Linic S, Aslam U, Boerigter C, et al. Photochemical transformations on plasmonic metal nanoparticles. ***Nature Materials***, 2015, 14(6), 567-576.

[9] Song J, Long J, Liu Y, et al. Highly efficient plasmon induced hot-electron transfer at Ag/TiO_2 Interface. ***ACS Photonics***, 2021, 8(5), 1497-1504.

[10] Wu K, Rodríguez-Córdoba W E, Yang Y, et al. Plasmon-induced hot electron transfer from the Au tip to CdS rod in CdS-Au nano-heterostructures. ***Nano Letters,*** 2013, 13(11), 5255-5263.

[11] Cheruvathoor Poulose, A., Zoppellaro, G., Konidakis, I., Serpetzoglou, E., Stratakis, E., Tomanec, O., ... & Zbořil, R. Fast and selective reduction of nitroarenes under visible light with an earth-abundant plasmonic photocatalyst. ***Nature Nanotechnology***, 2022, 17(5), 485-492.

[12] Ulmer, U., Dingle, T., Duchesne, P. N., Morris, R. H., Tavasoli, A., Wood, T., & Ozin, G. A. Fundamentals and applications of photocatalytic CO_2 methanation. ***Nature Communications***, 2019, 10(1), 3169.

[13] Cui, J., Li, Y., Liu, L., Chen, L., Xu, J., Ma, J., ... & Huang, Y. (2015). Near-infrared plasmonic-enhanced solar energy harvest for highly efficient photocatalytic reactions. ***Nano Letters***, 15(10), 6295-6301.

[14] Li, X., Zhang, X., Everitt, H. O., & Liu, J.. Light-induced thermal gradients in ruthenium catalysts significantly enhance ammonia production. ***Nano Letters***, 2019, 19(3), 1706-1711.

[15] Kim, M., Lee, J. H., & Nam, J. M. Plasmonic photothermal nanoparticles for biomedical applications. ***Advanced Science***, 2019, 6(17), 1900471.

[16] Avalos-Ovando, O., Besteiro, L. V., Movsesyan, A., Markovich, G., Liedl, T., Martens, K., ... & Govorov, A. O. Chiral photomelting of dna-nanocrystal assemblies utilizing plasmonic photoheating. ***Nano Letters***, 2021, 21(17), 7298-7308.

[17] Zhou, L., Tan, Y., Ji, D., Zhu, B., Zhang, P., Xu, J., ... & Zhu, J. Self-assembly of highly efficient, broadband plasmonic absorbers for solar steam generation. ***Science Advances***, 2016, 2(4), e1501227.

[18] Neumann, O., Urban, A. S., Day, J., Lal, S., Nordlander, P., & Halas, N. J. Solar vapor generation enabled by nanoparticles. ***ACS Nano***, 2013, 7(1), 42-49.

[19] Liu, C., Huang, J., Hsiung, C. E., Tian, Y., Wang, J., Han, Y., & Fratalocchi, A. High-performance large-scale solar steam generation with nanolayers of reusable biomimetic nanoparticles. ***Advanced Sustainable Systems***, 2017, 1(1-2), 1600013.

[20] Mascaretti, L., Schirato, A., Fornasiero, P., Boltasseva, A., Shalaev, V. M., Alabastri, A., &

Naldoni, A. Challenges and prospects of plasmonic metasurfaces for photothermal catalysis. ***Nanophotonics***, 2022, 11(13), 3035-3056.

[21] Li, Y., Lin, C., Li, K., Chi, C., & Huang, B. Nanoparticle-on-Mirror Metamaterials for Full-Spectrum Selective Solar Energy Harvesting. ***Nano Letters,*** 2022, 22(14), 5659-5666..

[22] Stewart J W, Nebabu T, Mikkelsen M H. Control of Nanoscale Heat Generation with Lithography-Free Metasurface Absorbers. ***Nano Letters***, 2022, 22(13): 5151-5157.

[23] Yu, N., & Capasso, F. Flat optics with designer metasurfaces. ***Nature Materials***, 2014, 13(2), 139-150.

[24] Qin, F., Ding, L., Zhang, L., Monticone, F., Chum, C. C., Deng, J., ... & Qiu, C. W. Hybrid bilayer plasmonic metasurface efficiently manipulates visible light. ***Science Advances***, 2016, 2(1), e1501168.

[25] Chen, H. T., Taylor, A. J., & Yu, N. A review of metasurfaces: physics and applications. ***Reports on Progress in Physics***, 2016, 79(7), 076401.

[26] Neshev, D. N., & Miroshnichenko, A. E. Enabling smart vision with metasurfaces. ***Nature Photonics***, 2023, 17(1), 26-35.

[27] Daqiqeh Rezaei, S., Dong, Z., You En Chan, J., Trisno, J., Ng, R. J. H., Ruan, Q., ... & Yang, J. K. Nanophotonic structural colors. ***ACS Photonics***, 2020, 8(1), 18-33.

[28] Li, W., & Valentine, J. Metamaterial perfect absorber based hot electron photodetection. ***Nano Letters***, 2014, 14(6), 3510-3514.

[29] Guan, J., Park, J. E., Deng, S., Tan, M. J., Hu, J., & Odom, T. W. Light–Matter Interactions in Hybrid Material Metasurfaces. ***Chemical Reviews***, 2022, 122(19), 15177-15203.

[30] Yang, J., Sun, Q., Ueno, K., Shi, X., Oshikiri, T., Misawa, H., & Gong, Q. Manipulation of the dephasing time by strong coupling between localized and propagating surface plasmon modes. ***Nature Communications***, 2018, 9(1), 4858.

[31] Baranov, D. G., Munkhbat, B., Zhukova, E., Bisht, A., Canales, A., Rousseaux, B., ... & Shegai, T. (2020). Ultrastrong coupling between nanoparticle plasmons and cavity photons at ambient conditions. ***Nature Communications***, 2020, 11(1), 2715.

[32] Li, W., Guler, U., Kinsey, N., Naik, G. V., Boltasseva, A., Guan, J., ... & Kildishev, A. V. Refractory plasmonics with titanium nitride: broadband metamaterial absorber. ***Advanced Materials***, 2014, 26(47), 7959-7965.

[33] Nishijima, Y., To, N., Balčytis, A., & Juodkazis, S. Absorption and scattering in perfect thermal radiation absorber-emitter metasurfaces. ***Optics Express***, 2022, 30(3), 4058-4070.

[34] Chen, K., Adato, R., & Altug, H. Dual-band perfect absorber for multispectral plasmon-enhanced infrared spectroscopy. 2012, ***ACS Nano***, 6(9), 7998-8006.

[35] Mao, P., Liu, C., Niu, Y., Qin, Y., Song, F., Han, M., ... & Zhang, S. Disorder-Induced Material-Insensitive Optical Response in Plasmonic Nanostructures: Vibrant Structural Colors from Noble Metals. ***Advanced Materials***, 2021, 33(23), 2007623.

[36] Mao, P., Liu, C., Song, F., Han, M., Maier, S. A., & Zhang, S. Manipulating disordered plasmonic systems by external cavity with transition from broadband absorption to reconfigurable reflection. ***Nature Communications***, 2020, 11(1), 1538.

[37] Baffou, G. and R. Quidant, ***Thermoplasmonics, in World Scientific Handbook of Metamaterials and Plasmonics: Volume 4: Recent Progress in the Field of Nanoplasmonics***. 2018, World Scientific. P 379-407.

[38] Baffou, G., R. Quidant, and F.J. García de Abajo, Nanoscale control of optical heating in complex plasmonic systems. ***ACS Nano***, 2010, 4(2), 709-716.

[39] Chen, X., Chen, Y., Yan, M., & Qiu, M. Nanosecond photothermal effects in plasmonic nanostructures. ***ACS Nano***, 2012, 6(3), 2550-2557.

[40] Jiang, Y., Chen, J. A., Du, Z., Liu, F., Qin, Y., Mao, P., & Han, M.. Gas phase fabrication of morphology-controlled ITO nanoparticles and their assembled conductive films. ***Nanoscale***, 2023, 15(8), 3907-3918.

[41] Mao, P., Liu, C., Favraud, G., Chen, Q., Han, M., Fratalocchi, A., & Zhang, S. Broadband single molecule SERS detection designed by warped optical spaces. ***Nature Communications***, 2018, 9(1), 5428.

[42] Siddique, R. H., Gomard, G., & Hölscher, H. The role of random nanostructures for the omnidirectional anti-reflection properties of the glasswing butterfly. ***Nature Communications***, 2015, 6(1), 6909.

[43] Hart, T. R., Aggarwal, R. L., & Lax, B. Temperature dependence of Raman scattering in silicon. ***Physical Review B***, 1970, 1(2), 638.

[44] Liu, M. S., Bursill, L. A., Prawer, S., Nugent, K. W., Tong, Y. Z., & Zhang, G. Y. Temperature dependence of Raman scattering in single crystal GaN films. ***Applied Physics Letters***, 1999,

74(21), 3125-3127.

[45] Calizo, I., Balandin, A. A., Bao, W., Miao, F., & Lau, C. N. Temperature dependence of the Raman spectra of graphene and graphene multilayers. ***Nano Letters***, 2007, 7(9), 2645-2649.

[46] Jorio, A., Dresselhaus, G., Dresselhaus, M. S., Souza, M., Dantas, M. S. S., Pimenta, M. A., ... & Cheng, H. M. Polarized Raman study of single-wall semiconducting carbon nanotubes. ***Physical Review Letters***, 2000, 85(12), 2617.

[47] Uchida, T., Tachibana, M., Kurita, S., & Kojima, K. Temperature dependence of the Breit–Wigner–Fano Raman line in single-wall carbon nanotube bundles. ***Chemical Physics Letters***, 2004, 400(4-6), 341-346.

[48] Dresselhaus, M. S., Dresselhaus, G., Jorio, A., Souza Filho, A. G., & Saito, R. Raman spectroscopy on isolated single wall carbon nanotubes. ***Carbon***, 2002, 40(12), 2043-2061.

[49] Peercy, P.S. and B. Morosin, Pressure and Temperature Dependences of the Raman-Active Phonons in SnO_2. ***Physical Review B***, 1973, 7(6), 2779-2786.

[50] Sahoo, S., Chitturi, V. R., Agarwal, R., Jiang, J. W., & Katiyar, R. S. Thermal conductivity of freestanding single wall carbon nanotube sheet by Raman spectroscopy. ***ACS Applied Materials & Interfaces***, 2014, 6(22), 19958-19965.

[51] Endo, M., Uchiyama, H., Ohno, Y., & Hirotani, J. Temperature dependence of Raman shift in defective single-walled carbon nanotubes. ***Applied Physics Express***, 2022, 15(2), 025001..

TOC Graphic

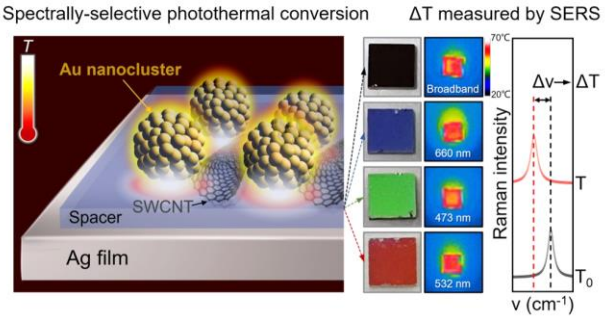
Spectrally-selective photothermal conversion
ΔT measured by SERS
T
Au nanocluster
SWCNT
Spacer
Ag film
Broadband
660 nm
473 nm
532 nm
70°C
20°C
Raman intensity
Δν
ΔT
T
T0
ν (cm-1)